Geochemical Perspectives Letters

Final assembly of Gondwana enhances crustal metal (HREE and U) endowment

P. Liu[1,2*], S.A. Gleeson[2,3], N.J. Cook[4], B. Lehmann[5], C. Zhao[6], W. Yao[1], Z.A. Bao[1], S.T. Wu[7], Y.F. Tian[8], J.W. Mao[8]

https://doi.org/10.7185/geochemlet.2317

Abstract

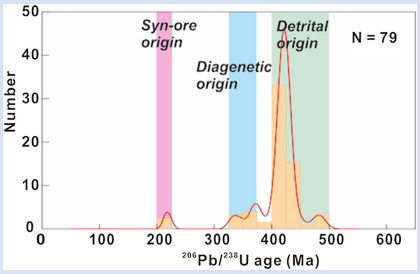

The South China Block hosts a variety of U and HREE mineralisation styles. The Yushui Cu deposit is located at a sedimentary unconformity and is enriched in HREEs and U. U-Pb ages of uraninite and xenotime indicate that the HREE mineralisation is epigenetic and formed at *ca.* 223 ± 1 Ma. Ore petrography, elemental mapping, and Nd isotope data suggest that HREEs and U were leached from the footwall sandstone and transported to the Cu deposit *via* oxidised basinal brines. U-Pb ages of detrital xenotime and zircon from the sandstone show that this sedimentary sequence was mainly derived from Silurian S-type granites, which were emplaced during Gondwana amalgamation. Rapid erosion formed clastic sedimentary rocks that contain accessory HREE-U minerals which could be remobilised by younger mineralising events. S-type granite magmatism during the final assembly of Gondwana established the crustal metal reservoir which was repeatedly tapped over geological history, including the modern formation of regolith hosted HREE deposits in South China. Given the global distribution of analogous S-type granites in other terranes globally, our study has exploration implications outside of China. This will be enlightening for finding new HREE deposits, which is vital to support the transition to a low carbon footprint energy.

Received 13 March 2023 | Accepted 3 May 2023 | Published 26 May 2023

Introduction

Genetic relationships between ore formation and crustal evolution are long established (Sawkins, 1984; Cawood and Hawkesworth, 2015). These relationships may, however, be difficult to identify due to the interplay between multiple geological processes (*e.g.*, magmatism, sedimentary processes, and weathering) and the complexity of crustal evolution. Sediment hosted ore deposits commonly display evidence for a protracted sequence of mineralising events stretching from sedimentation to diagenesis to post-diagenetic metamorphism and/or metasomatism (Hitzman *et al.*, 2005). Thus, these systems can help elucidate the relationship between ore formation and crustal evolution.

Although detrital zircon U-Pb geochronology of clastic sedimentary rocks is a well established tool for reconstructing crustal evolution (Košler *et al.*, 2002), xenotime U-Pb geochronology provides a unique glimpse into not only sedimentary sources (*e.g.*, detrital xenotime; Kositcin *et al.*, 2003) but also into the post-depositional history of the sedimentary sequences (*e.g.*, diagenetic xenotime; McNaughton *et al.*, 1999). Xenotime is a widespread heavy rare earth (HREE) mineral which can form by magmatic, sedimentary, and hydrothermal processes but typically has small grain sizes (<20 μm); this has previously hampered routine U-Pb dating of xenotime. However, recent advances in microanalytical *in situ* U-Pb dating methods have improved the spatial resolution (~10 μm) achievable by laser ablation inductively coupled plasma mass spectrometry (LA-ICP-MS) (Wu *et al.*, 2020). Contemporary microanalysis thus can circumvent the common problem of small grain size (<20 μm) and allows routine U-Pb xenotime dating of clastic sedimentary rocks.

We present *in situ* LA-ICP-MS U-Pb ages for xenotime and uraninite from the Yushui deposit (South China), a sediment hosted high grade Cu deposit. We integrate these data with petrography and Nd isotope data for the footwall sandstone, and propose that the HREEs and U were leached from the red footwall sandstone *via* oxidised basinal brines. The U-Pb dates from clastic xenotime and detrital zircon show that the footwall sandstone is mainly sourced from Silurian S-type granites, which

1. State Key Laboratory of Continental Dynamics, Department of Geology, Northwest University, Xi'an 710069, China
2. GFZ German Research Centre for Geosciences, Potsdam 14473, Germany
3. Institute of Geological Sciences, Freie Universität Berlin, Berlin 14463, Germany
4. School of Chemical Engineering, The University of Adelaide, South Australia 5005, Australia
5. Mineral Resources, Clausthal University of Technology, Clausthal–Zellerfeld 38678, Germany
6. School of Earth Science and Resources, Chang'an University, Xi'an 710054, China
7. Institute of Geology and Geophysics, Chinese Academy of Sciences, Beijing 100029, China
8. MNR Key Laboratory for Exploration Theory and Technology of Critical Mineral Resources, China University of Geosciences, Beijing, 100083, China
* Corresponding author (email: pengliu@nwu.edu.cn)

were formed in the South China block when it represented the northern margin of East Gondwana. Given that the amalgamation of Gondwana is the most important period of S-type granite production in geological history, we suggest that the final assembly of Gondwana enhanced crustal metal (HREE and U) endowment in China, but also worldwide. Therefore, similar processes may be important in other S-type granite provinces, a finding that carries significant global implications for rare earth exploration, which can be further pivotal to pursuing a successful green energy transition.

Geological Background and Samples

The Yushui Cu deposit is located in eastern Guangdong Province. The economically important bedded/massive mineralisation is hosted at an unconformity between the lower Carboniferous red sandstone of the Zhongxin Formation and a dark grey dolostone/limestone of the upper Carboniferous Hutian Formation (Fig. S-1). The >300 m thick Zhongxin Formation comprises hematite-bearing red sandstone with abundant detrital minerals including xenotime, rutile, and zircon (Figs. 1b, S-2a–c). The Hutian Formation is predominantly composed of >350 m thick dolomite and limestone with organic- and apatite-rich beds in the lower part (Fig. S-2d). The bedded/massive mineralisation comprises Cu sulfides, barite, hematite, anhydrite, sphalerite, galena (Fig. S-2e,f), and U and HREE-rich minerals, with local HREE grades up to 6.1 wt. % (Fig. S-3, Table S-1). The HREE-rich domains include uraninite (Fig. 1c), hingganite-[Y] ($Y_2Be_2[SiO_4]_2[OH]_2$, Fig. 1d), thortveitite ($[Sc,Y]_2Si_2O_7$, Fig. 1e), jingwenite-[Y] ($Y_2Al_2V^{4+}{}_2[SiO_4]_2O_4[OH]_4$, Fig. 1f; Liu *et al.*, 2023), xenotime (Fig. 1g), iimoriite-[Y] ($Y_2[SiO_4]$ $[CO_3]$, Fig. S-4a), synchysite-[Y] ($CaY[CO_3]_2F$, Fig. S-4b), kamphaugite-[Y] ($CaY[CO_3]_2[OH]\cdot H_2O$, Fig. S-4c), and chernovite-[Y] ($Y[AsO_4]$, Fig. S-4d). Samples with hingganite-[Y], uraninite, and xenotime were collected from the bedded/massive mineralisation, and detrital zircon and xenotime were sampled from the lower Carboniferous red sandstone. There are three types of xenotime grains in the sandstone: xenotime-(I) occurring as anhedral grains intergrown with hematite forming veinlets (Fig. S-4e), xenotime-(II) occurring as fine grained (5–15 μm) anhedral grains (Fig. S-4f), and xenotime-(III) occurring as euhedral to subhedral grains intergrown with detrital zircon and quartz (Figs. S-2c, S-4g,h). Sample details are given in Figure S-5; analytical methods in Supplementary Information.

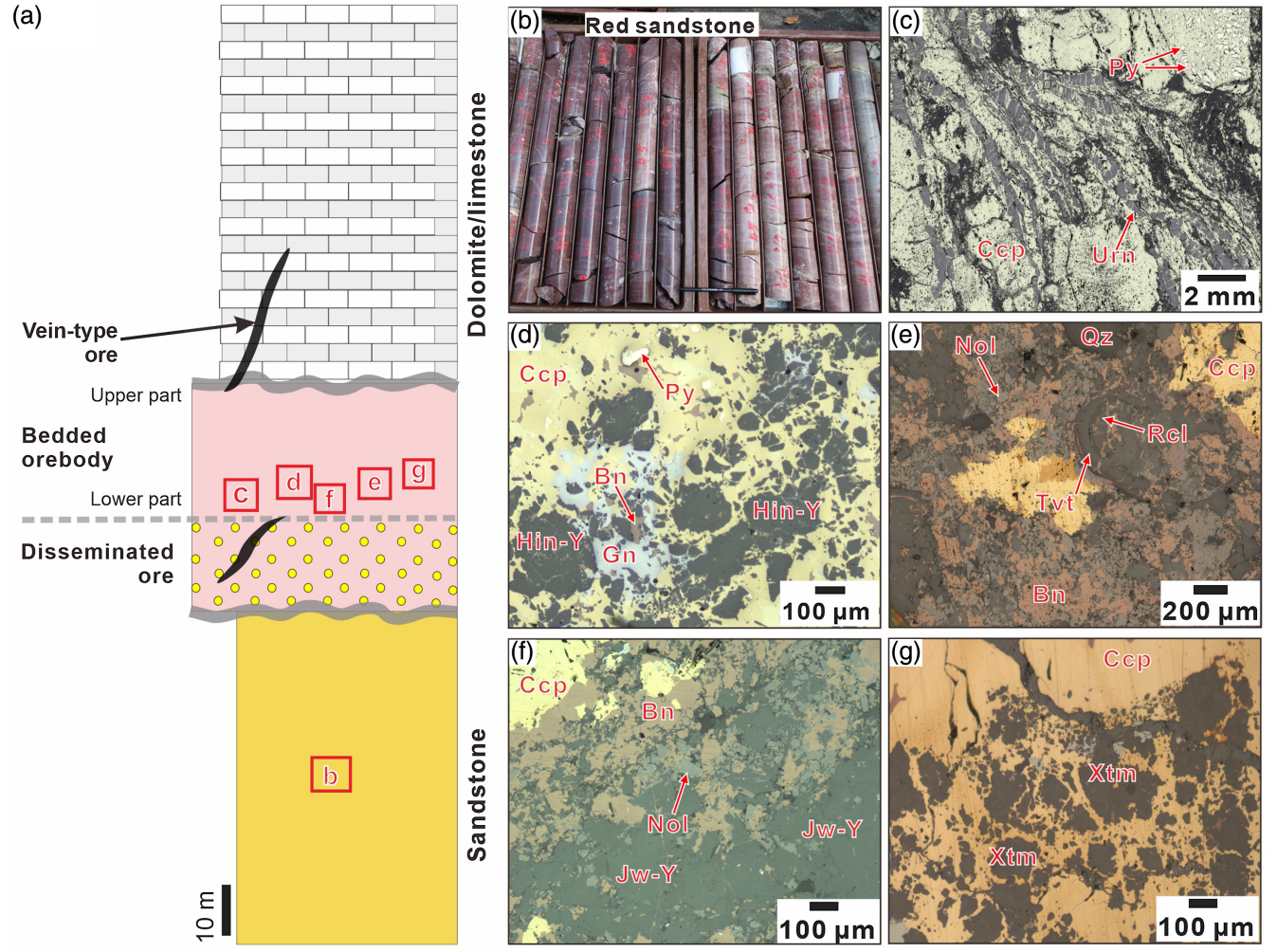

Figure 1 **(a)** Stratigraphic column of the Yushui deposit. **(b)** Photographs of the red sandstone. **(c–g)** Reflected light photomicrographs showing the HREE- and U-bearing minerals from the bedded mineralisation. **(c)** Elongated aggregates of uraninite, **(d)** subhedral hingganite–[Y] grains, **(e)** anhedral roscoelite and colloidal thortveitite, **(f)** agglomerate of euhedral jingwenite–[Y], and **(g)** subhedral xenotime grains in a matrix of bornite and chalcopyrite. Bn, bornite; Ccp, chalcopyrite; Hin–Y, hingganite–[Y]; Gn, galena; Jw–Y, jingwenite–[Y]; Nol, nolanite; Py, pyrite; Qz, quartz; Rcl, roscoelite; Tvt, thortveitite; Urn, uraninite; Xtm, xenotime.

Results

In situ U-Pb dating of xenotime, zircon, and uraninite. Fifty seven spot analyses of 26 uraninite grains yielded a weighted mean $^{206}Pb/^{238}U$ age of 223.7 ± 0.8 Ma (2σ, MSWD = 0.7) (Fig. 2a, Table S-2). Thirty spot analyses of 25 xenotime grains from the bedded/massive orebody returned a lower intercept age of 221.8 ± 3.5 Ma (2σ, MSWD = 2.2) on a Tera-Wasserburg plot. The ^{207}Pb corrected $^{206}Pb/^{238}U$ ages yielded a weighted mean of 222.4 ± 2.4 Ma (2σ, MSWD = 1.5) (Fig. 2b, Table S-2).

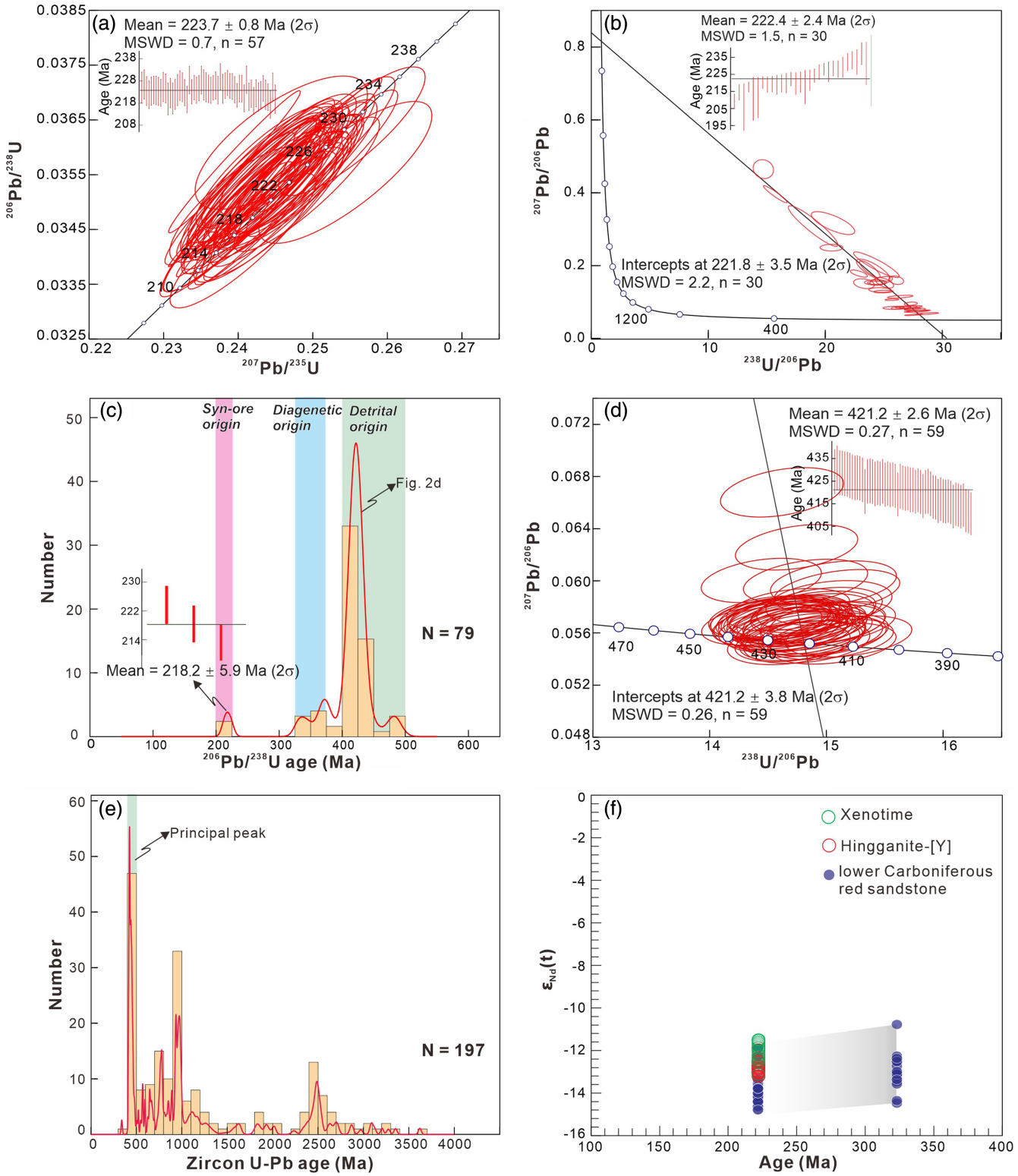

Figure 2 **(a–e)** LA-ICP-MS U-Pb isotope diagrams of **(a)** uraninite and **(b)** xenotime from the bedded mineralisation, **(c, d)** xenotime and **(e)** detrital zircon from the footwall red sandstone. **(c)** and **(d)** show ages for xenotime from the red sandstone. Three spot analyses on xenotime-I yielded a weighted mean age **(c)**, and fifty nine spots on xenotime-III returned a lower intercept age and weighted corrected age **(d)**. **(f)** $\varepsilon_{Nd}(t)$ *vs. t* plot of the red sandstone, and the hingganite-[Y] and xenotime from the bedded mineralisation.

Seventy nine spot analyses of xenotime-I, -II, and -III from the footwall red sandstone yielded three ranges of U-Pb ages at 228–218 Ma ($n = 3$), 387–329 Ma ($n = 11$), and 486–404 Ma ($n = 65$) (Fig. 2c, Table S-3), respectively. Three spot analyses on xenotime-I with the range at 228–218 Ma yielded a weighted mean $^{206}Pb/^{238}U$ age of 218.2 ± 5.9 Ma. Fifty nine spot analyses on xenotime-III from the major peak at 431–404 Ma returned a lower intercept age of 421.2 ± 3.8 Ma (2σ, MSWD = 0.26) on the Tera-Wasserburg plot, and a ^{207}Pb corrected weighted mean $^{206}Pb/^{238}U$ age of 421.2 ± 2.6 Ma (2σ, MSWD = 0.27) (Fig. 2d). 197 spot analyses of detrital zircon of the footwall red sandstone yielded three major peaks at 470–410 Ma ($n = 45$), 1100–900 Ma ($n = 42$), and 2600–2300 Ma ($n = 24$) (Fig. 2e, Table S-4).

In situ and bulk rock Sm-Nd isotope composition. Thirty *in situ* spot analyses on 30 hingganite-[Y] grains yielded a Sm-Nd isochron age of 233 ± 12 Ma (2σ, MSWD = 0.8) (Fig. S-6a, Table S-5). Twenty one *in situ* spot analyses on 20 xenotime grains from the orebody returned a Sm-Nd isochron age of 225 ± 26 Ma (2σ, MSWD = 0.19) (Fig. S-6b, Table S-5), similar to the U-Pb age of 222.4 ± 2.4 Ma within uncertainty. The $\varepsilon_{Nd}(t)$ values of hingganite-[Y] and xenotime were calculated using an age of 223 Ma, and range from −13.2 to −12.0 and −13.3 to −11.4, respectively (Fig. 2f). Bulk rock Sm-Nd isotope analyses of the lower Carboniferous red sandstone yielded $^{143}Nd/^{147}Nd$ values ranging from 0.511747 to 0.512008 (Table S-5). Initial $\varepsilon_{Nd}(t)$ values were calculated using the formation ages of 323 Ma for the red sandstone, ranging from −14.5 to −10.8 (Fig. 2f).

Discussion

Source of rare earths and uranium. This contribution focuses on the genesis of the HREE and U mineralisation of the Yushui Cu deposit. The new combined radioisotopic data from multiple minerals provide a consistent dataset with a concordant mineral formation age of *ca*. 223 ± 1 Ma. This age corresponds to a period of significant post-orogenic extension of the South China block (Zhao *et al.*, 2018). There is no magmatism at Yushui coeval with HREE and U mineralisation.

The $\varepsilon_{Nd}(t)$ values (−13.3 to −11.4) of HREE minerals from the unconformity at Yushui are consistent with those (−14.8 to −10.8) of the underlying red sandstone. Abundant detrital heavy minerals such as xenotime, monazite, rutile, and zircon occur in the footwall red sandstone sequence. These minerals show dissolution and alteration textures (Fig. S-7), which indicate fluid leaching of HREEs and U. This is also supported by the Y, Yb, and U distributions revealed by EPMA elemental mapping of xenotime in the red sandstone (Fig. 3).

Genetic links between unconformity-related U deposits and HREE mineralisation have been proposed elsewhere, for example in the Northern Territory, Australia (Nazari-Dehkordi *et al.*, 2018; Richter *et al.*, 2018), and the Athabasca Basin, Saskatchewan, Canada (Quirt *et al.*, 1991; Fayek and Kyser, 1997). Both these examples formed in extensional settings *via* the large scale circulation of oxidised, relatively low temperature saline fluids, with ore deposition taking place at redox interfaces (Quirt *et al.*, 1991; Fayek and Kyser, 1997; Nazari-Dehkordi *et al.*, 2018; Richter *et al.*, 2018). Similar fluids have been identified in primary fluid inclusions at Yushui (*i.e.* 8–15 wt. % NaCl equiv., 110–287 °C; Jiang *et al.*, 2016). In general, the hydrothermal transport of REEs requires complexation with a dominance of Cl^-, CO_3^{2-}, and SO_4^{2-} species (Williams-Jones *et al.*, 2012; Migdisov *et al.*, 2016; Zhou *et al.*, 2016). The occurrence of hydrothermal barite, anhydrite, hematite, synchysite-[Y], kamphaugite-[Y], and iimoriite-[Y] in the Yushui mineralisation indicates that the ore fluids were oxidised with a dominance of CO_3^{2-} and SO_4^{2-}. However, although redox reactions cannot effectively drive the formation of HREE-bearing minerals (Migdisov *et al.*, 2016), the presence of phosphorus in hydrothermal fluids can significantly lower the solubilities of HREEs (Williams-Jones *et al.*, 2012; Gysi *et al.*, 2015), and, notably, there are apatite-rich beds in the lower part of the overlying dolostone/limestone at Yushui. Therefore, we suggest that HREEs and U were leached from detrital minerals in the underlying hematite-bearing red sandstone by saline, oxidised basinal fluids

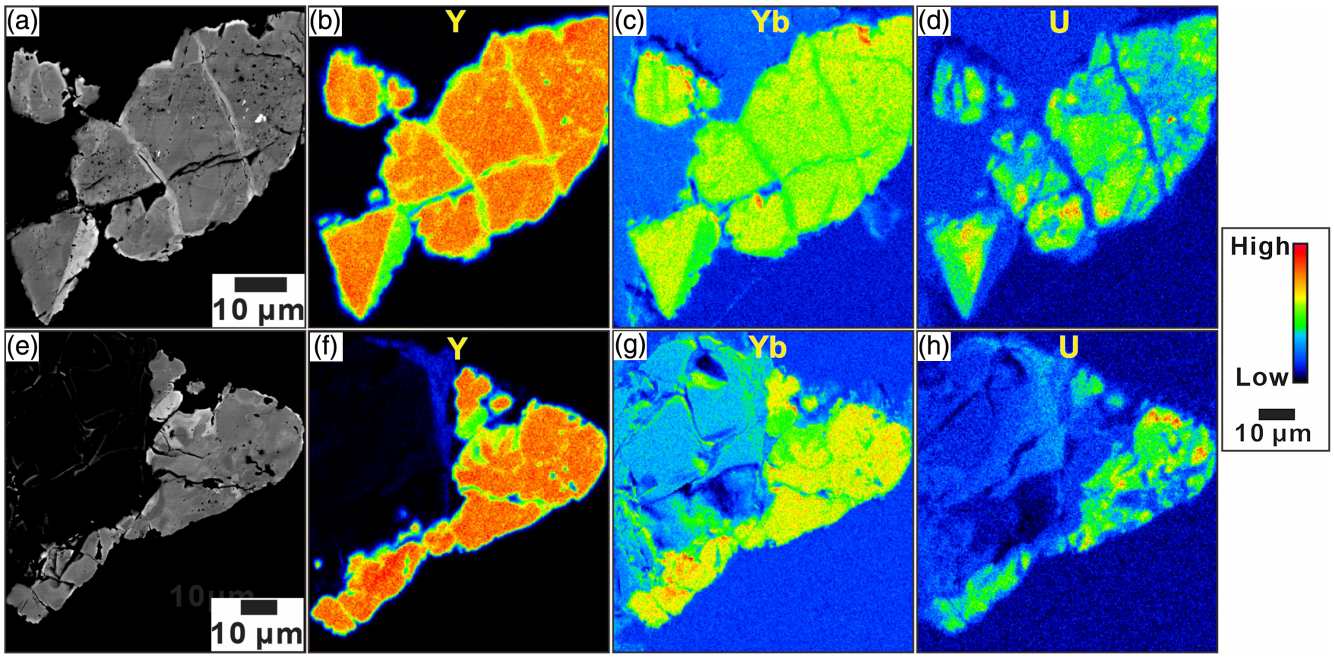

Figure 3 **(a, e)** Backscattered electron (BSE) images and electron probe microanalysis (EPMA) element maps of clastic xenotime in red sandstone, showing the distributions and textures of leaching of **(b, f)** Y, **(c, g)** Yb, and **(d, h)** U.

and were then precipitated in organic-rich beds in the overlying dolostone/limestone, which acted as a reductant and also provided P for efficient REE fixation.

Metal Endowment from the Final Assembly of Gondwana

The age range of 228–218 Ma for xenotime-I from the footwall red sandstone is coeval with the formation age (223 Ma) of HREE- and U-bearing minerals from the bedded mineralisation. The 387–329 Ma range for xenotime-II is comparable to the formation age of the Late Devonian to early Carboniferous sedimentary sequence. By contrast, the 486–404 Ma age range for detrital xenotime-III is coincident with the principal age peak at 470–410 Ma of detrital zircon in the footwall sandstone. The Devonian to Carboniferous successions in the South China block are dominated by siliciclastic units with minor coeval magmatism (Wang *et al.*, 2010), and contain significant amounts of detrital xenotime, monazite, rutile, and zircon. Triassic extension produced rifting-related, basinal fluid circulation and leaching of metals (*e.g.*, HREEs and U) by oxidised basinal fluids from the underlying red sandstone sequence. Notably, Late Devonian to early Carboniferous sedimentary red bed basins are found elsewhere (Song *et al.*, 2017), such as the Chu-Sarysu basin of Kazakhstan, which also hosts major redox-controlled U deposits (Dahlkamp, 2009). Therefore, this finding strongly suggests that analogous Carboniferous red bed sedimentary basins in South China and elsewhere may also host HREE and U mineralisation.

Crucially, the principal peak (421.2 ± 2.6 Ma) of detrital xenotime corresponds to the age of Silurian S-type granites in South China (Zhao *et al.*, 2018), suggesting that the footwall sandstone is ultimately derived from Silurian S-type granites. Such granites in South China are mainly peraluminous two mica/garnet granites. They have been interpreted as a far field response to early Palaeozoic continental collision and then orogenic collapse events (Wang *et al.*, 2010) (Fig. 4a), which led to the South China block becoming accreted to the northern margin of East Gondwana leading to the final Gondwana assembly (Fig. 4b) (Cawood *et al.*, 2013; Zhao *et al.*, 2018).

S-type granites generally have a metapelitic source characterised by accessory assemblages comprising xenotime, monazite, and zircon (Chappell *et al.*, 1987; Bea and Montero, 1999). Partial melting of metapelites can enhance the HREE and U concentrations in peraluminous melts (Bea and Montero, 1999; Villaseca *et al.*, 2003). In addition, P has a high solubility in strongly peraluminous S-type granitic magmas and there is substitution of $REE^{3+} + Y^{3+}$ for Zr ($ZrSiO_4 \leftrightarrow [REE,Y]PO_4$) in zircon from S-type granites which is charge balanced by P^{5+} (Burnham and Berry, 2017). Consequently, subsequent crystallisation of the S-type granites would produce abundant zircon, xenotime, and monazite.

The amalgamation of Gondwana is the most important period of S-type granite production in geological history, especially in Australia, Europe, and South China (Spencer *et al.*, 2014; Zhu *et al.*, 2020). Rapid erosion led to clastic sedimentary rocks that contain abundant HREE-U-bearing minerals which can then be leached by younger mineralising events. Furthermore,

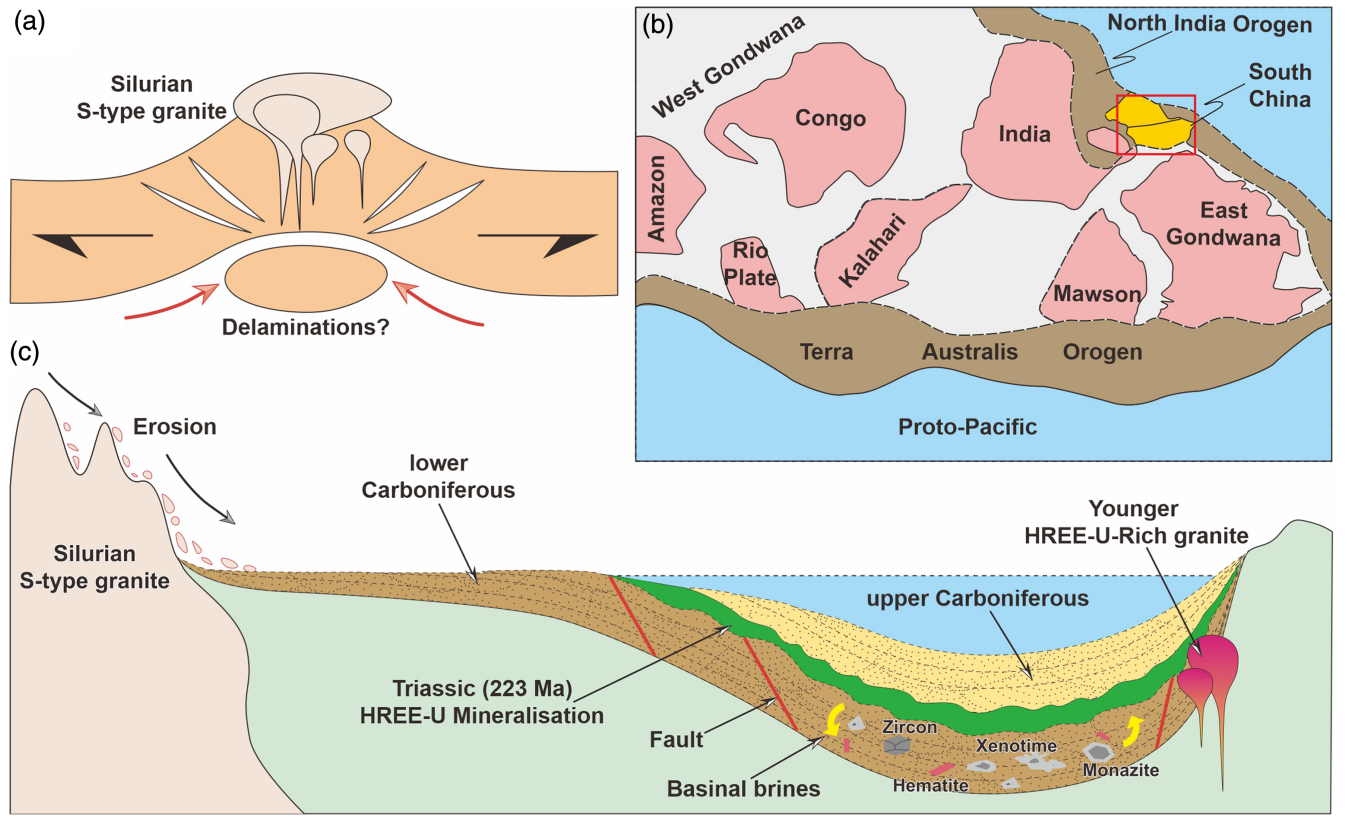

Figure 4 **(a)** Schematic genetic model of Silurian S-type granites as a far field response to early Palaeozoic continental collision and orogenic collapse events. **(b)** Schematic palaeogeographic reconstruction showing the position of the South China block during the Gondwana assembly (Cawood *et al.*, 2013). **(c)** Genetic model of erosion of Silurian S-type granites to form the lower Carboniferous red sandstone with abundant detrital zircon, xenotime, and monazite. Then Triassic extension allowed basinal fluid circulation, resulting in leaching of metals (*e.g.*, HREEs and U) from the red sandstone sequence.

these HREE-U-bearing clastic sedimentary rocks may undergo partial melting and generate younger HREE-U-rich granites (Fig. 4c) which may then be upgraded by processes in the critical zone to form the recent/subrecent regolith-hosted (or ion adsorption) HREE deposits of South China (Li *et al.*, 2017). Our study highlights that the final assembly of Gondwana established a long term metal reservoir in South China which was tapped repeatedly by ore forming fluids.

Acknowledgements

This research was jointly funded by the National Natural Science Foundation of China (Grants 42272070 and 42130102), the Young Star of Science and Technology Plan Projects in Shaanxi Province, China (Grant 2023KJXX-037) and the Natural Science Basic Research Program in Shaanxi Province of China (2022JC-DW5-01). PL is funded by the China Scholarship Council. SAG is funded by a Helmholtz Recruitment Initiative.

Editor: Raúl Fonseca

Additional Information

Supplementary Information accompanies this letter at https://www.geochemicalperspectivesletters.org/article2317.

Cite this letter as: Liu, P., Gleeson, S.A., Cook, N.J., Lehmann, B., Zhao, C., Yao, W., Bao, Z.A., Wu, S.T., Tian, Y.F., Mao, J.W. (2023) Final assembly of Gondwana enhances crustal metal (HREE and U) endowment. *Geochem. Persp. Let.* 26, 7–13. https://doi.org/10.7185/geochemlet.2317

References

Bea, F., Montero, P. (1999) Behavior of accessory phases and redistribution of Zr, REE, Y, Th, and U during metamorphism and partial melting of metapelites in the lower crust: an example from the Kinzigite Formation of Ivrea-Verbano, NW Italy. *Geochimica et Cosmochimica Acta* 63, 1133–1153. https://doi.org/10.1016/S0016-7037(98)00292-0

Burnham, A.D., Berry, A.J. (2017) Formation of Hadean granites by melting of igneous crust. *Nature Geoscience* 10, 457–461. https://doi.org/10.1038/ngeo2942

Cawood, P.A., Hawkesworth, C.J. (2015) Temporal relations between mineral deposits and global tectonic cycles. In: Jenkin, G.R.T., Lusty, P.A.J., Mcdonald, I., Smith, M.P., Boyce, A.J., Wilkinson, J.J. (Eds.) *Ore Deposits in an Evolving Earth*. Geological Society, London, Special Publication 393, Geological Society of London, 9–21. https://doi.org/10.1144/SP393.1

Cawood, P.A., Wang, Y., Xu, Y., Zhao, G. (2013) Locating South China in Rodinia and Gondwana: A fragment of greater India lithosphere? *Geology* 41, 903–906. https://doi.org/10.1130/G34395.1

Chappell, B.W., White, A.J.R., Wyborn, D. (1987) The Importance of Residual Source Material (Restite) in Granite Petrogenesis. *Journal of Petrology* 28, 1111–1138. https://doi.org/10.1093/petrology/28.6.1111

Dahlkamp, F.J. (2009) *Uranium Deposits of the World: Asia*. Springer-Verlag, Berlin, Heidelberg. https://doi.org/10.1007/978-3-540-78558-3

Fayek, M., Kyser, T.K. (1997) Characterization of multiple fluid-flow events and rare-earth-element mobility associated with formation of unconformity-type uranium deposits in the Athabasca Basin, Saskatchewan. *The Canadian Mineralogist* 35, 627–658. https://pubs.geoscienceworld.org/canmin/article-pdf/35/3/627/3420516/627.pdf

Gysi, A.P., Williams-Jones, A.E., Harlov, D. (2015) The solubility of xenotime-(Y) and other HREE phosphates ($DyPO_4$, $ErPO_4$, and $YbPO_4$) in aqueous solutions from 100 to 250 °C and p_{sat}. *Chemical Geology* 401, 83–95. https://doi.org/10.1016/j.chemgeo.2015.02.023

Hitzman, M., Kirkham, R., Broughton, D., Thorson, J., Selley, D. (2005) The Sediment-Hosted Stratiform Copper Ore System. In: Hedenquist, J.W., Thompson, J.F.H., Goldfarb, R.J., Richards, J.P. (Eds.) *Economic Geology One Hundreth Anniversary Volume*, Society of Economic Geologists, Inc., Littleton, Colorado, 609–642. https://doi.org/10.5382/AV100.19

Jiang, B.-b., Zhu, X.-y., Cheng, X.-y., Wang, H. (2016) Characteristics and geological significance of fluid inclusions in the Yushui copper polymetallic deposit, Guangdong Province. *Geology in China* 43, 2163–2172 (in Chinese with English abstract). http://doi.org/10.12029/gc20160624

Kositcin, N., McNaughton, N.J., Griffin, B.J., Fletcher, I.R., Groves, D.I., Rasmussen, B. (2003) Textural and geochemical discrimination between xenotime of different origin in the Archaean Witwatersrand Basin, South Africa. *Geochimica et Cosmochimica Acta* 67, 709–731. https://doi.org/10.1016/S0016-7037(02)01169-9

Košler, J., Fonneland, H., Sylvester, P., Tubrett, M., Pedersen, R.-B. (2002) U–Pb dating of detrital zircons for sediment provenance studies–a comparison of laser ablation ICPMS and SIMS techniques. *Chemical Geology* 182, 605–618. https://doi.org/10.1016/S0009-2541(01)00341-2

Li, Y.H.M., Zhao, W.W., Zhou, M.-F. (2017) Nature of parent rocks, mineralization styles and ore genesis of regolith-hosted REE deposits in South China: An integrated genetic model. *Journal of Asian Earth Sciences* 148, 65–95. https://doi.org/10.1016/j.jseaes.2017.08.004

Liu, P., Gu, X., Zhang, W., Hu, H., Chen, X., Wang, X., Song, W., Yu, M., Cook, N.J. (2023) Jingwenite-(Y) from the Yushui Cu deposit, South China: The first occurrence of a V-HREE-bearing silicate mineral. *American Mineralogist* 108, 192–196. https://doi.org/10.2138/am-2022-8373

McNaughton, N.J., Rasmussen, B., Fletcher, I.R. (1999) SHRIMP Uranium-Lead Dating of Diagenetic Xenotime in Siliciclastic Sedimentary Rocks. *Science* 285, 78–80. https://doi.org/10.1126/science.285.5424.78

Migdisov, A., Williams-Jones, A.E., Brugger, J., Caporuscio, F.A. (2016) Hydrothermal transport, deposition, and fractionation of the REE: Experimental data and thermodynamic calculations. *Chemical Geology* 439, 13–42. https://doi.org/10.1016/j.chemgeo.2016.06.005

Nazari-Dehkordi, T., Spandler, C., Oliver, N.H.S., Wilson, R. (2018) Unconformity-Related Rare Earth Element Deposits: A Regional-Scale Hydrothermal Mineralization Type of Northern Australia. *Economic Geology* 113, 1297–1305. https://doi.org/10.5382/econgeo.2018.4592

Quirt, D.H., Kotzer, T., Kyser, T.K. (1991) Tourmaline, phosphate minerals, zircon, and pitchblende in the Athabasca Group: Maw Zone and McArthur River areas, Saskatchewan. In: *Summary of Investigations 1991*. Saskatchewan Geological Survey, Saskatchewan Ministry of Energy and Mines, Miscellaneous Report 91-4, 181–191. https://pubsaskdev.blob.core.windows.net/pubsask-prod/88108/88108-Quirt-Kotzer-Kyser_1991_MiscRep91-4.pdf

Richter, L., Diamond, L.W., Atanasova, P., Banks, D.A., Gutzmer, J. (2018) Hydrothermal formation of heavy rare earth element (HREE)–xenotime deposits at 100 °C in a sedimentary basin. *Geology* 46, 263–266. https://doi.org/10.1130/G39871.1

Sawkins, F.J. (1984) *Metal Deposits in Relation to Plate Tectonics*. Springer, New York. https://doi.org/10.1007/978-3-642-96785-6

Song, H., Jiang, G., Poulton, S.W., Wignall, P.B., Tong, J., Song, H., An, Z., Chu, D., Tian, L., She, Z., Wang, C. (2017) The onset of widespread marine red beds and the evolution of ferruginous oceans. *Nature Communications* 8, 399. https://doi.org/10.1038/s41467-017-00502-x

Spencer, C.J., Cawood, P.A., Hawkesworth, C.J., Raub, T.D., Prave, A.R., Roberts, N.M.W. (2014) Proterozoic onset of crustal reworking and collisional tectonics: Reappraisal of the zircon oxygen isotope record. *Geology* 42, 451–454. https://doi.org/10.1130/G35363.1

Villaseca, C., Martín Romera, C., De la Rosa, J., Barbero, L. (2003) Residence and redistribution of REE, Y, Zr, Th and U during granulite-facies metamorphism: behaviour of accessory and major phases in peraluminous granulites of central Spain. *Chemical Geology* 200, 293–323. https://doi.org/10.1016/S0009-2541(03)00200-6

Wang, Y., Zhang, F., Fan, W., Zhang, G., Chen, S., Cawood, P.A., Zhang, A. (2010) Tectonic setting of the South China Block in the early Paleozoic: Resolving intracontinental and ocean closure models from detrital zircon U-Pb geochronology. *Tectonics* 29, TC6020. https://doi.org/10.1029/2010TC002750

Williams-Jones, A.E., Migdisov, A.A., Samson, I.M. (2012) Hydrothermal Mobilisation of the Rare Earth Elements – a Tale of "Ceria" and "Yttria". *Elements* 8, 355–360. https://doi.org/10.2113/gselements.8.5.355

Wu, S., Yang, M., Yang, Y., Xie, L., Huang, C., Wang, H., Yang, J. (2020) Improved *in situ* zircon U–Pb dating at high spatial resolution (5–16 μm) by laser ablation–single collector–sector field–ICP–MS using Jet sample and X skimmer cones. *International Journal of Mass Spectrometry* 456, 116394. https://doi.org/10.1016/j.ijms.2020.116394

Zhao, G., Wang, Y., Huang, B., Dong, Y., Li, S., Zhang, G., Yu, S. (2018) Geological reconstructions of the East Asian blocks: From the breakup of Rodinia to the assembly of Pangea. *Earth-Science Reviews* 186, 262–286. https://doi.org/10.1016/j.earscirev.2018.10.003

Zhou, L., Mavrogenes, J., Spandler, C., Li, H. (2016) A synthetic fluid inclusion study of the solubility of monazite-(La) and xenotime-(Y) in H_2O-Na-K-Cl-F-CO_2 fluids at 800 °C and 0.5 GPa. *Chemical Geology* 442, 121–129. https://doi.org/10.1016/j.chemgeo.2016.09.010

Zhu, Z., Campbell, I.H., Allen, C.M., Burnham, A.D. (2020) S-type granites: Their origin and distribution through time as determined from detrital zircons. *Earth and Planetary Science Letters* 536, 116140. https://doi.org/10.1016/j.epsl.2020.116140

Geochemical Perspectives Letters

Final assembly of Gondwana enhances crustal metal (HREE and U) endowment

P. Liu, S.A. Gleeson, N.J. Cook, B. Lehmann, C. Zhao, W. Yao, Z.A. Bao, S.T. Wu, Y.F. Tian, J.W. Mao

Supplementary Information

The Supplementary Information includes:

- Sample Descriptions
- Analytical Methods
- Supplementary Figures S-1 to S-7
- Supplementary Tables S-1 to S-5
- Supplementary Information References

Sample Descriptions

Three samples containing uraninite (sample 1804YS04), xenotime (sample1605YS04), and hingganite-[Y] (sample 1804YS10) for U-Pb dating, and Sm-Nd isotope analysis were collected from the lower part of the bedded orebody. Fourteen samples (Ys01-14) of sulfide bulk ore were collected from the lower to the upper part of the bedded orebody. Five samples (20YS11, 23, 26, 29, and 32) with clastic xenotime and one sample (20YS28) with detrital zircon of red sandstone for U-Pb dating, and sixteen samples of red sandstone for bulk-rock Sm-Nd isotope analysis were collected from the footwall red sandstone (sampling locations are shown in Fig. S-5). The xenotime, hingganite-[Y], and uraninite samples were prepared as polished sections for element mapping, U-Pb dating, Sm-Nd analysis. Detrital zircon samples were handpicked under a binocular microscope, mounted in an epoxy resin disc, and then polished for U-Pb dating analysis. Hingganite-[Y] and xenotime in the bedded mineralisation occur as subhedral to anhedral grains, uraninite occurs as elongated aggregates (Figs. 1c–g and S-4d, e), and detrital zircon in the sandstone occur as euhedral to subhedral grains. The xenotime, hingganite-[Y], and uraninite samples were prepared as polished sections for element mapping and U-Pb dating analysis. The element mapping of xenotime was carried out by electron probe microanalysis (EPMA), and the U-Pb data were acquired by LA-ICP-MS. *In-situ* xenotime and hingganite-[Y], and bulk-rock Sm-Nd isotope data were acquired by LA-MC-ICP-MS and MC-ICP-MS, respectively.

Analytical Methods

μ-XRF element mapping

Element mapping was carried out at Guangzhou Tuoyan Analytical Technology Co., Ltd., China, using a Bruker's M4 Tornado Plus μ-XRF spectrometer. The X-ray generator was operated at 50 kV and 300 μA and a composition of filters was used to reduce the background. All measurements were carried out under 2 mbar vacuum conditions and directly on the samples which were placed on the μ-XRF platform with pixel distance for 18 μm and a 5 ms time per pixel. Evaluation of the data and preparation of element distribution maps were done using M4 TORNADO software provided by Bruker Nano Analytics.

SEM and mineral and element mapping

Mineral/phase distribution maps were obtained on thin sections using a TESCAN Integrated Mineral Analyser (TIMA3 GHM) system at the State Key Laboratory of Continental Dynamics, Northwest University, Xi'an, China. The measurements were performed with the dot-mapping mode. Pixel spacing (BSE) was set to 3 μm and dot spacing (EDS) was set to 9 μm. All measurements were done at 25 kV with a spot size of 50 nm in high-vacuum mode, a working distance of 15 mm and beam current of 5 nA. EPMA element mapping was carried out using a JEOL JXA-8230 electron microprobe with an accelerating voltage of 15 kV, beam current of 50 nA, and beam diameter of 1 μm.

LA-ICP-MS U-Pb xenotime dating

U-Pb isotopic analysis of xenotime hosted in the bedded/massive mineralisation was carried out using an Analytikjena M90 quadrupole ICP-MS equipped with a 193 nm NWR193 Ar-F excimer laser at Yanduzhongshi Geological Analysis Laboratories, China. Each analysis incorporated a background acquisition of approximately 20 s followed by 40 s of data acquisition from the sample. Each analysis was performed with a spot size diameter of 15 μm at 7 Hz with an energy of 4 J/cm^2. The reference xenotime material (MG-1) was analysed twice for every six analyses as an external standard, and the xenotime reference (BS-1, 513.6 ± 4.5 Ma; Liu *et al*., 2011) was analysed once for every six analyses as a control standard sample to check age reproducibility. U-Pb isotope analysis of xenotime hosted in the red sandstone was done using an Element XR HR-ICP-MS instrument (Thermo Fisher Scientific, USA) coupled with a 193 nm Ar-F excimer laser system (Geolas HD, Göttingen, Germany) at the State Key Laboratory of Lithospheric Evolution, Institute of Geology and Geophysics, Chinese Academy of Sciences. Each analysis was performed with a spot size of 10 μm at 2 Hz with an energy of 5 J/cm^2. Possible surface contamination was avoided by pre-ablation with two laser pulses. More details are given in Wu *et al*. (2020). The reference xenotime material (MG-1) was analysed twice for every six analyses as an external standard, and the xenotime reference (BS-1) was analysed once for every six analyses as a control standard to check age reproducibility. All measured isotope ratios of the MG-1 reference material during analyses were regressed and corrected via the method of Liu *et*

al. (2011). Isotopic and elemental fractionation plus instrumental mass bias were calibrated using Glitter 4.0 software (Griffin *et al*., 2008). The U-Pb ages and weighted mean ages were calculated using the ISOPLOT 3.0 software package (Ludwig, 2003).

LA-ICP-MS uraninite U-Pb dating

U-Pb dating of uraninite was conducted by LA-ICP-MS at the Wuhan Sample Solution Analytical Technology Co., Ltd., Wuhan, China, using an Agilent 7700e ICP-MS instrument coupled with a GeolasPro laser ablation system. Each analysis was performed with a spot size diameter of 10 μm at 1 Hz. Uraninite reference material (GBW04420) was used as an external standard for U-Pb isotope calibration. Each analysis incorporated a background acquisition of approximately 20–30 s followed by 50 s of data acquisition for the sample. The U-Pb ages were processed by ICPMSDataCal software (Liu *et al*., 2008), and the calculation of U-Pb ages was performed by the ISOPLOT 3.0 software package (Ludwig, 2003).

LA-MC-ICP-MS Sm-Nd isotope analysis

Neodymium isotopic ratios of hingganite-[Y] and xenotime were analysed by LA-MC-ICP-MS at Nanjing FocuMS Technology Co. Ltd, Jiangsu province, China, using a Nu Instruments *Nu Plasma II* MC-ICP-MS coupled with a RESOlution 193-nm ArF Excimer Laser Ablation system. For hingganite-[Y] and xenotime Sm-Nd isotope analyses, each acquisition incorporated 20 s background (gas blank). Each analysis was performed with a spot size diameter of 75 μm at 5 Hz with an energy of 4.5 J/cm^2. To correct for this interference of ^{144}Sm on ^{144}Nd, the ^{147}Sm/^{149}Sm ratio (1.0868) and the measured ^{147}Sm/^{149}Sm ratios are for calculating the Sm fractionation factor, and then the measured ^{147}Sm intensity and the natural ^{147}Sm/^{144}Sm ratios are used for correcting the Sm interference on mass 144. The interference-corrected ^{146}Nd/^{144}Nd ratios were then normalised to 0.7219 for calculating the Nd fractionation factor. The ^{143}Nd/^{144}Nd and ^{145}Nd/^{144}Nd ratios were normalised via the exponential law. Standard monazites (Trebilcock, M4, 44069, M2 and Namaqualand-2) and apatites (AP1, MAD, OtterLake, Durango, and AP2) were used as quality control for every ten unknown samples. Similarly, the ^{147}Sm/^{144}Nd ratios were calculated by the exponential law after correction of the isobaric interference of ^{144}Sm on ^{144}Nd, and was externally calibrated against the ^{147}Sm/^{144}Nd ratio of the standard monazite (Namaqualand-2, ^{147}Sm/^{144}Nd = 0.0980 ± 3; Liu *et al*., 2012).

Bulk-rock Nd isotope analysis

High-precision Nd isotope measurements were done at Nanjing FocuMS Technology Co. Ltd, Jiangsu province (China), using a Nu Instruments Nu Plasma II MC-ICP-MS. Rock powders were mixed with 0.5 mL 60 wt. % HNO_3 and 1.0 mL 40 wt. % HF in high-pressure PTFE bombs. Digested samples were dried down on a hotplate and reconstituted in 1.5 mL of 1.5 N HCl before ion exchange purification. Biorad AG50W-X8 cation exchange column was for roughly separating Sr and REE. High-field-strength-elements were washed out by 1.5 N HCl, and matrix elements (Na, Mg, K, Ca) and Rb were followed by 2.0 N HCl; then the Sr and

REE fractions were washed out by 2.5 and 6.0 N HCl, respectively. After that REE fractions were dried down, re-dissolved in 0.12 N HCl, and loaded onto LN-specific columns. La, Ce, and Pr were washed out by 0.12 N HCl, and then Nd and Sm were eluted by 0.18 and 0.4 N HCl, respectively. Small aliquots of each sample solution were analysed for exacting element concentration by Agilent Technologies 7700x quadrupole ICP-MS. Raw data of Nd isotope ratios were corrected for mass fractionation via normalising to $^{146}Nd/^{144}Nd = 0.7219$ with exponential law. An isotope standard (JNdi-1) was used to correct instrumental drift. Reference materials (USGS BHVO-2, BCR-2, RGM-2, AVG-2,) were used as quality-control standards.

Bulk-rock REE analysis of sulfide ore

REE analyses of bulk ore were done by an Agilent 7700e ICP-MS at Nanjing FocuMS Technology Co. Ltd, Jiangsu province, China. About 40 mg powder was mixed with 0.5 mL 60 wt. % HNO_3 and 1.0 mL 40 % HF in high-pressure PTFE bombs. To ensure complete digestion, the bombs were steel-jacketed and placed in the oven at 195 °C for 3–4 days. Then the bombs were opened, solutions dried down on a hotplate, re-dissolved with 5 mL 15 wt. % HNO_3 and 1 mL Rh internal standard, sealed and placed in the oven at 150 °C. Aliquots of the digestions were nebulised into an Agilent Technologies 7700x quadrupole ICP-MS to analyse trace elements. Geochemical USGS reference materials for quality control were basalt (BCR-2, BHVO-2), rhyolite (RGM-2), andesite (AVG-2), and granodiorite (GSP-2).

LA-ICP-MS zircon U-Pb dating

SEM imaging and LA-ICP-MS zircon U-Pb dating of zircon was obtained at the State Key Laboratory of Continental Dynamics, Northwest University, Xi'an, using a TESCAN Integrated Mineral Analyser (TIMA3 GHM) system and an Agilent 7900 ICP-MS coupled with a RESOlution M-50 193-nm ArF Excimer Laser Ablation system, respectively. Based on observations of internal textures, inclusion- and fracture-free zircon grains were selected for U-Pb dating. Each analysis was performed with a uniform spot size diameter of 37 μm at 5 Hz with an energy of 6 J/cm^2. NIST SRM 610 was analysed once for every six analyses of the tested sample. The reference zircon (GJ-1) was analysed twice for every six analyses as an external standard, and the reference zircon (Plesovice) was analysed once for every six analyses as a control standard to check data reproducibility. More detailed analytical procedures are given in Yuan *et al.* (2004). The U-Pb ages were processed by ICPMSDataCal software (Liu *et al*., 2008) and the calculation of U-Pb ages was performed by the ISOPLOT 3.0 software package (Ludwig, 2003).

Supplementary Figures

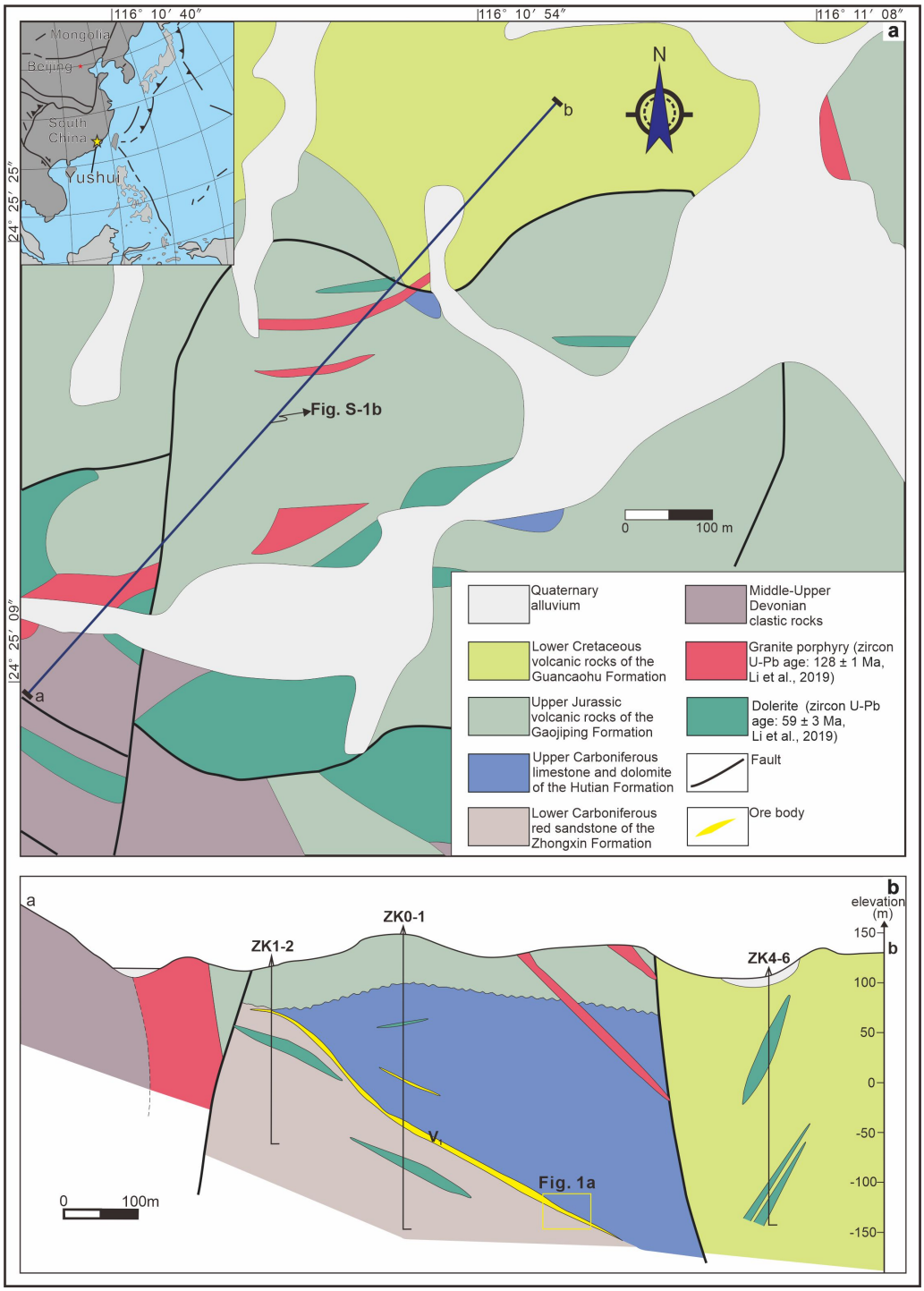

Figure S-1 **(a)** Geological map of the Yushui deposit (Huang *et al.*, 2015). **(b)** Geological cross section of the exploration line a–b in the Yushui deposit (Chen *et al.*, 2021). Zircon U-Pb data are from Li *et al.* (2019). V_1 is the main orebody.

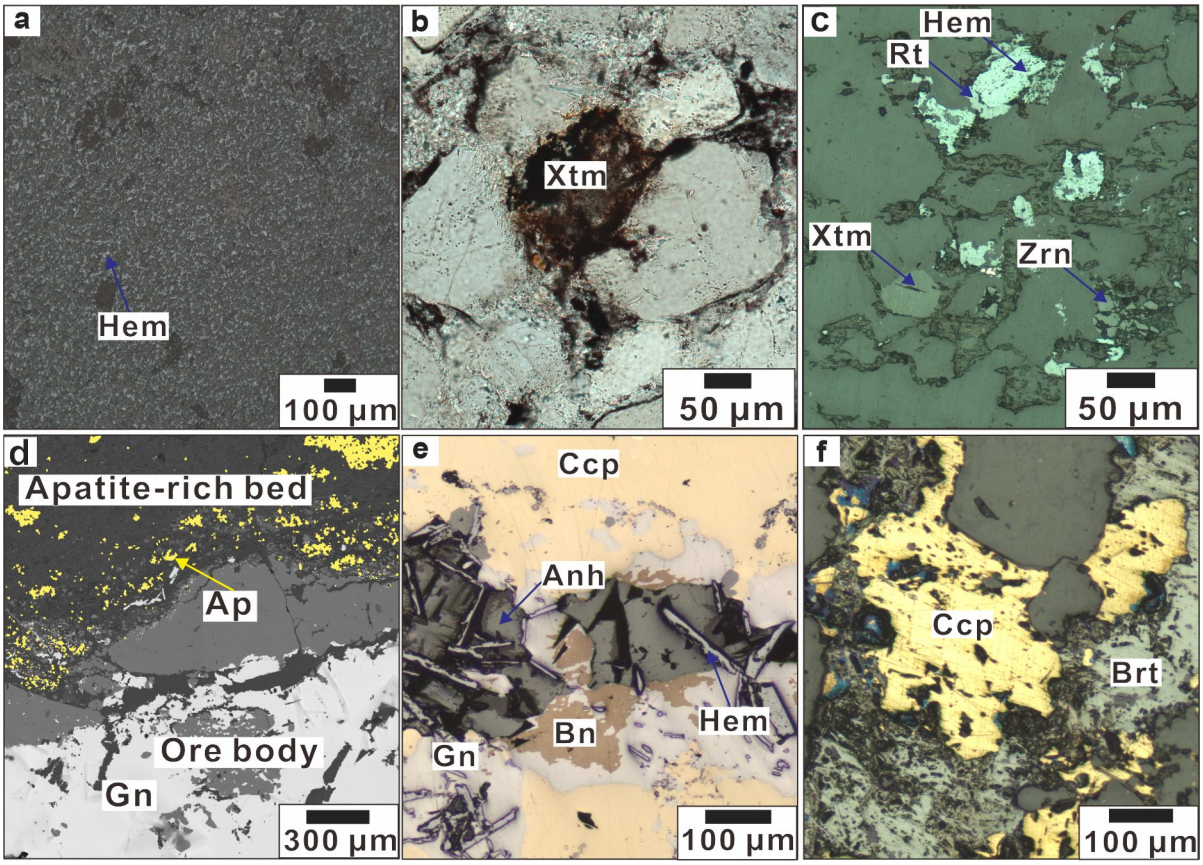

Figure S-2 **(a)** Reflected-light photomicrograph of hematite in the red sandstone. **(b)** Transmitted-light photomicrograph of xenotime in the red sandstone. **(c)** Reflected-light photomicrograph of hematite, xenotime, rutile, and zircon in the red sandstone. **(d)** SEM-EDS spectral image of apatite-rich beds in the overlying dolostone. **(e, f)** Reflected-light photomicrographs of anhydrite barite, hematite, and chalcopyrite in the bedded mineralisation. Abbreviations: Anh, anhydrite; Ap, apatite; Bn, bornite; Brt, barite; Ccp, chalcopyrite; Gn, galena; Hem, hematite; Rt, rutile; Qz, quartz; Xtm, xenotime; Zrn, zircon.

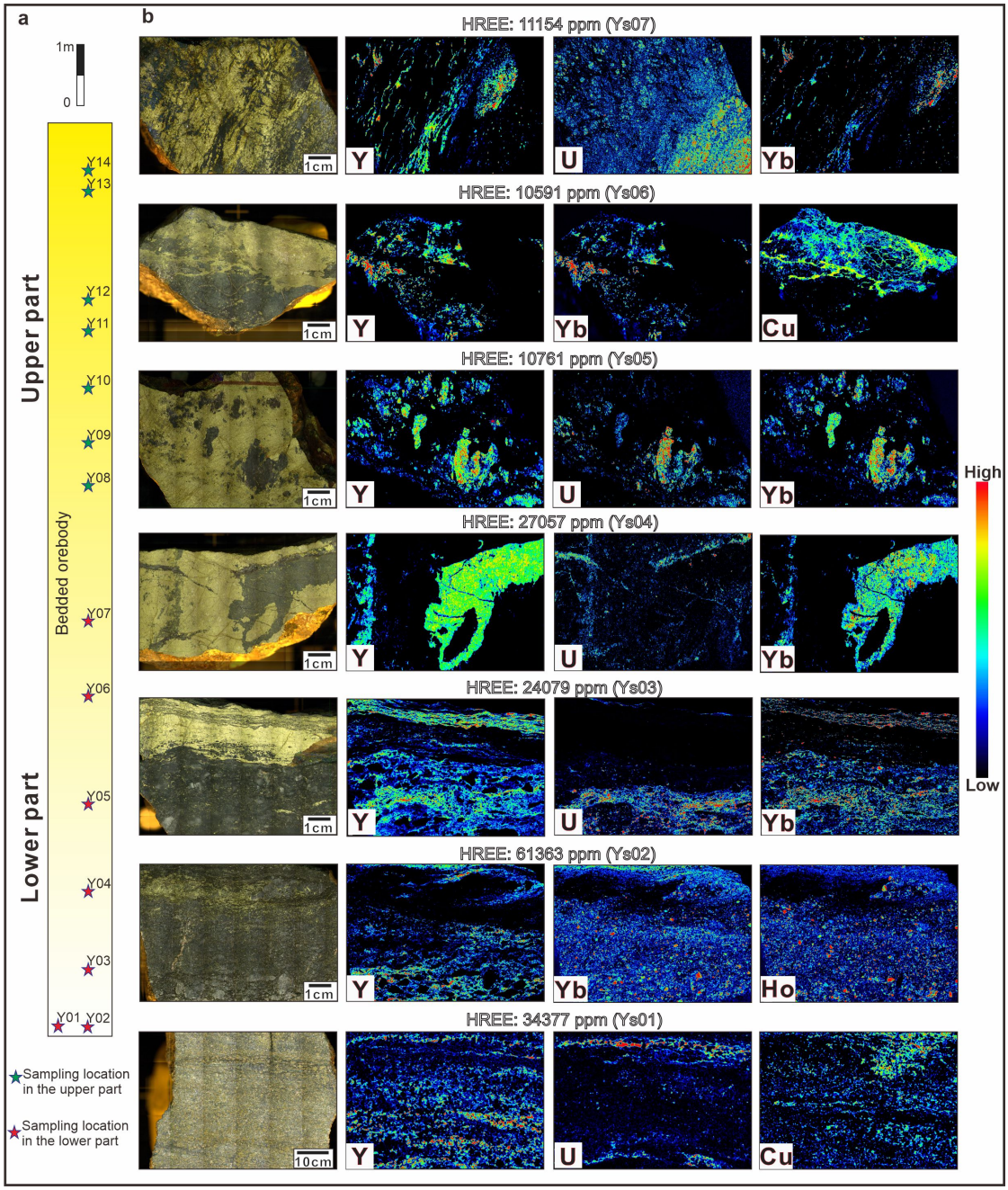

Figure S-3 Photographs of sulfide ore samples and μ-XRF images from the bedded orebody (about 10 m thick) at the Yushui deposit. **(a)** Sampling locations of fourteen bulk ore samples from the bedded orebody. **(b)** μ-XRF images and HREE concentrations of seven bulk ore samples (Ys01-07) from the lower part of the bedded orebody. Seven bulk ore samples from the lower part of the bedded/massive have high ∑REE and HREE concentrations of 1.1–6.6 × 10^4 ppm and 1.1–6.1 × 10^4 ppm, respectively, with a relatively high average HREE concentration of 2.5 × 10^4 ppm. Seven bulk ore samples from the upper part of bedded/massive mineralisation display relatively low ∑REE and HREE concentrations of 2.6–6.6 × 10^3 ppm and 2.3–5.4 × 10^3 ppm (Table S-1).

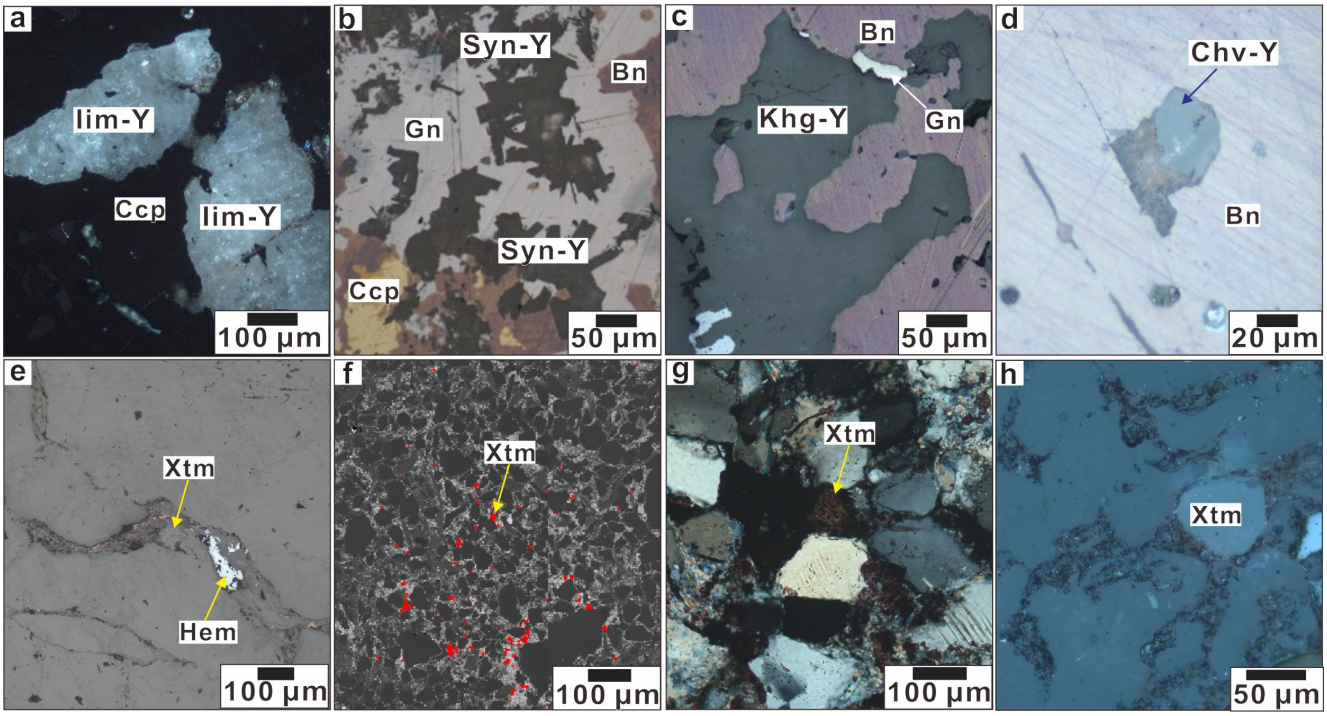

Figure S-4 **(a–d)** Photomicrographs of **(a)** iimoriite-[Y], **(b)** synchysite-[Y], **(c)** kamphaugite-[Y], and **(d)** chernovite-[Y] in a matrix of bornite and chalcopyrite. **(e–h)** Photomicrographs and SEM-EDS spectral image of xenotime in the footwall red sandstone. **(e)** Anhedral xenotime-I grains intergrown with hematite in a veinlet. **(f)** SEM-EDS spectral image of anhedral fine-grained xenotime-II grains. **(g, h)** Euhedral to subhedral xenotime-III grains. Abbreviations: Bn, bornite; Ccp, chalcopyrite; Chv-[Y], chernovite-[Y]; Gn, galena; Hem, hematite; Khg-[Y], kamphaugite-[Y]; Iim-[Y], iimoriite-[Y]; Syn-[Y], synchysite-[Y]; Xtm, xenotime.

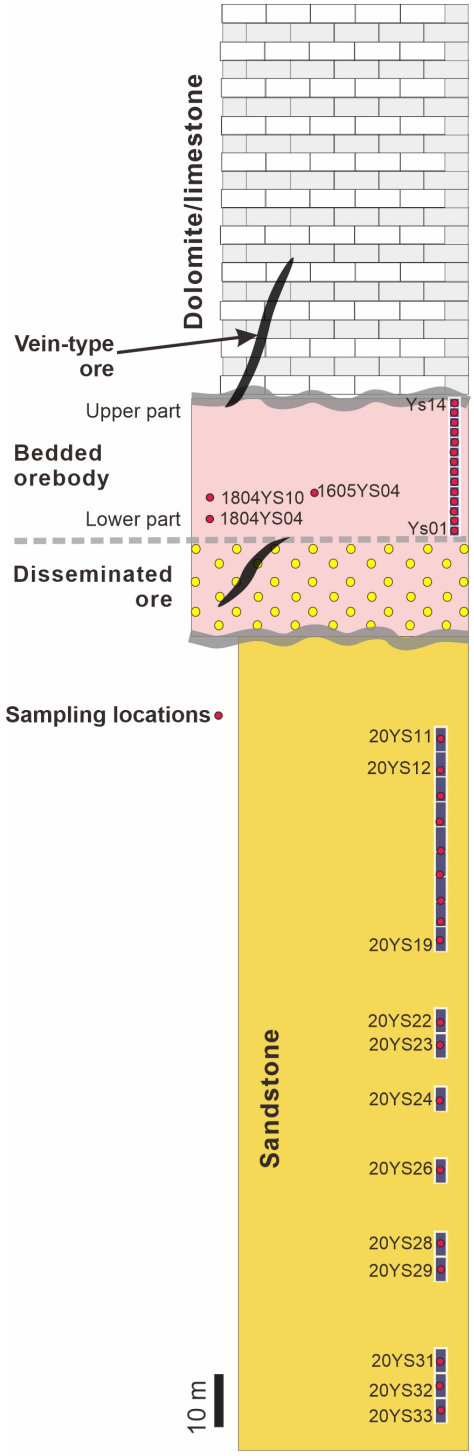

Figure S-5 Sketch figure showing sampling locations. Samples of hingganite-[Y] (1804YS04), uraninite (1804YS10), and xenotime-[Y] (1605YS04) were collected from the lower part of the bedded/massive orebody, 14 samples of sulfide bulk ore were collected from the bedded orebody from lower (Ys01) to upper part (Ys14). 16 samples for bulk-rock Nd isotope, 1 sample (20YS28) for detrital zircon U-Pb, and 5 samples (20YS11, 23, 26, 29 and 32) for clastic xenotime U-Pb analyses were taken from the footwall red sandstone.

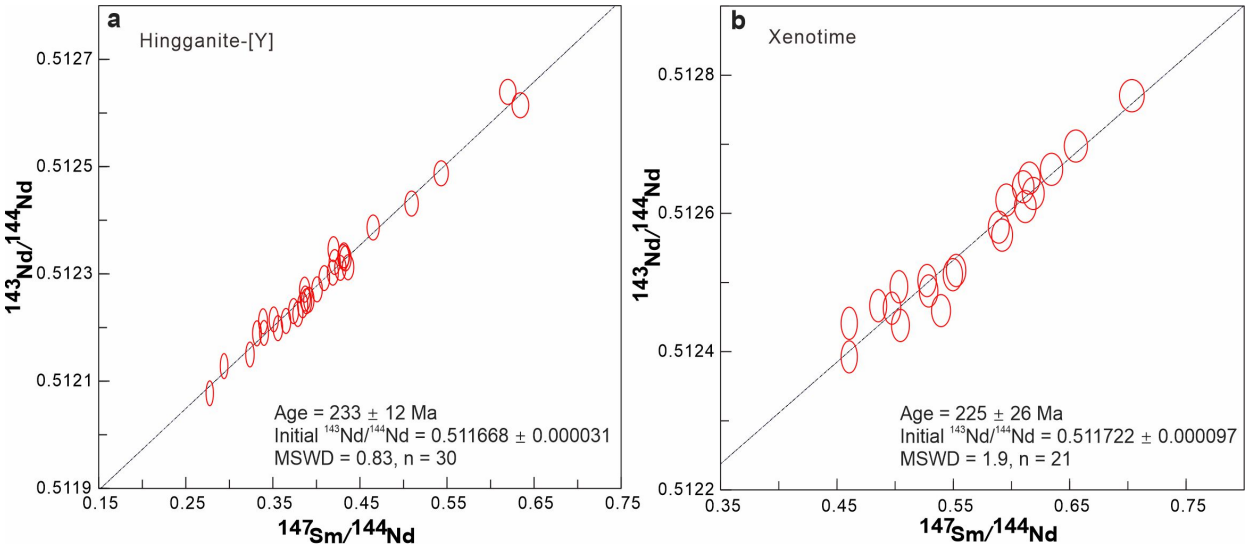

Figure S-6 Sm-Nd isochron plot of **(a)** hingganite-[Y] and **(b)** xenotime from the bedded mineralisation.

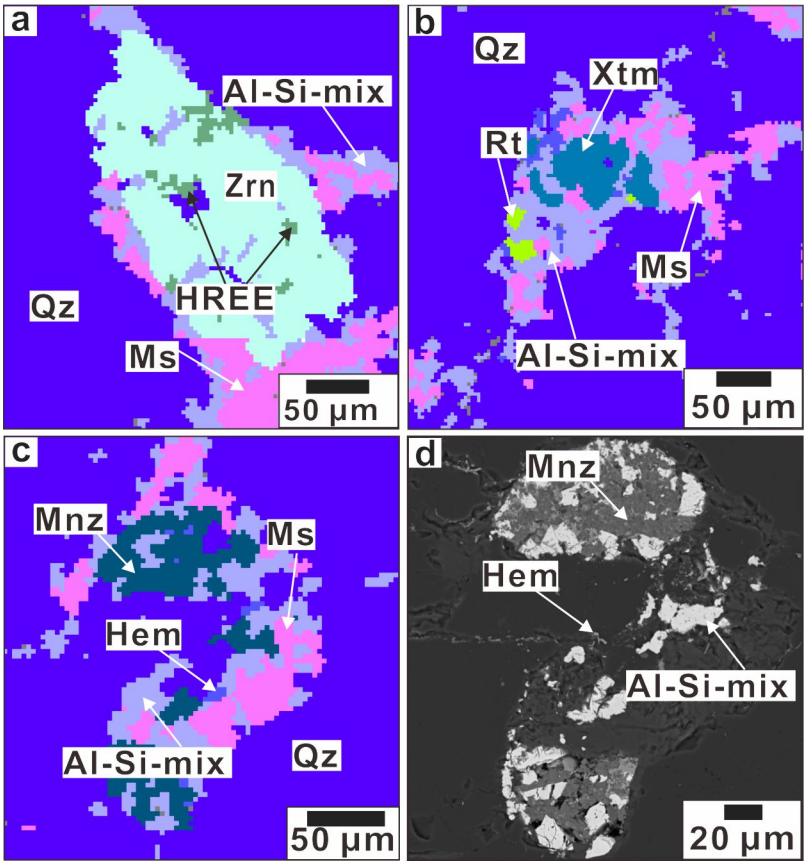

Figure S-7 SEM-EDS spectral images of **(a)** zircon, **(b)** xenotime, and **(c, d)** monazite in the red sandstone, showing dissolution-modification textures, and as-yet unidentified HREE-bearing and Al-Si-mix mineral phases within fluid-modified zircon, xenotime, and monazite. Abbreviations: Al-Si-mix, Aluminosilicate mixture; Hem, hematite; HREE, unidentified/unnamed HREE-bearing mineral phases; Mnz, monazite; Rt, rutile; Qz, quartz; Xtm, xenotime; Zrn, zircon.

Supplementary Tables

Table S-1 REE contents in bedded sulfide ore samples from the Yushui deposit (in ppm).

Table S-2 LA-ICP-MS U-Pb data of xenotime and uraninite in the ore samples. Samples 1804YS04 (uraninite) and 1605YS04 (xenotime) are from the lower part of the bedded mineralization.

Table S-3 LA-ICP-MS U-Pb data of xenotime-I, -II, and -III from the red sandstone of drillcore (ZK01).

Table S-4 LA-ICP-MS U-Pb data of detrital zircon samples from the red sandstone in drillcore (ZK01). Ages older than 1000 Ma were calculated using $^{207}Pb/^{206}Pb$ ratios, and ages younger than 1000 Ma were calculated using $^{206}Pb/^{238}U$ ratios.

Table S-5 Sm-Nd isotope data of hingganite-[Y] (1804YS10), xenotime (1605YS04), and lower Carboniferous red sandstone from the Yushui deposit. Samples 1804YS10 and 1605YS04 are from the lower part of the bedded mineralization, and 16 samples of the red sandstone are from drillcore (ZK01).

Tables S-1 through S-5 (.xlsx) are available for download from the online version of this article at https://doi.org/10.7185/geochemlet.2317.

Supplementary Information References

Chen, M., Ke, C., Tian, Y., Chen, G., Ma, K., Ma, S., Peng, Y., Zhang, W. (2021) Sedimentary-exhalative massive sulfide deposits in shallow marine environment: a case study from Yushui copper deposit, Guangdong Province. *Acta Geologica Sinica* 95, 1774–1791 (in Chinese with English abstract). https://caod.oriprobe.com/articles/61489376/Sedimentary_exhalative_massive_sulfide_deposits_in.htm

Griffin, W.L., Powell, W.J., Pearson, N.J., O'Reilly, S.Y. (2008) GLITTER: Data reduction software for laser ablation ICP-MS. In: Sylvester, P. (Eds.) *Laser Ablation ICP-MS in the Earth Sciences: Current Practices and Outstanding Issues*. Mineralogical Association of Canada Short Course Series v40, Mineralogical Association of Canada, Quebec, 308–311.

Huang, Y., Sun, X., Shi, G., Sa, R., Guang, Y., Jiang, X., Que, H. (2015) Re–Os dating of sulphides from the Yushui Cu-polymetallic deposit in eastern Guangdong Province, South China. *Ore Geology Reviews* 70, 281–289. https://doi.org/10.1016/j.oregeorev.2015.04.018

Li, S.-S., Chen, H.-Y., Peng, Y.-X., Wang, L.-M., Luo, Z.-R. (2019) Tectonic evolution of the Yongmei depression constrained by zircon LA-ICP-MS U-Pb ages of granite porphyry and diabase from the Yushui Cu-Pb-Zn polymetallic deposit. *Geochimica* 48, 313–324 (in Chinese with English abstract). https://doi.org/10.19700/j.0379-1726.2018.06.011.

Liu, Y., Hu, Z., Gao, S., Günther, D., Xu, J., Gao, C., Chen, H. (2008) *In situ* analysis of major and trace elements of anhydrous minerals by LA-ICP-MS without applying an internal standard. *Chemical Geology* 257, 34–43. https://doi.org/10.1016/j.chemgeo.2008.08.004

Liu, Z.C., Wu, F.Y., Guo, C.L., Zhao, Z.F., Yang, J.H., Sun, J.F. (2011) *In situ* U-Pb dating of xenotime by laser ablation (LA)-ICP-MS. *Chinese Science Bulletin* 56, 2948–2956. https://doi.org/10.1007/s11434-011-4657-y

Liu, Z.-C., Wu, F.-Y., Yang, Y.-H., Yang, J.-H., Wilde, S.A. (2012) Neodymium isotopic compositions of the standard monazites used in U–Th–Pb geochronology. *Chemical Geology* 334, 221–239. https://doi.org/10.1016/j.chemgeo.2012.09.034

Ludwig, K.R. (2003) User's Manual for Isoplot/Ex Version 3.00. A Geochronological Toolkit for Microsoft Excel. *Berkeley Geochronology Center Special Publication* 4, 77 p.

Wu, S., Yang, M., Yang, Y., Xie, L., Huang, C., Wang, H., Yang, J. (2020) Improved *in situ* zircon U–Pb dating at high spatial resolution (5–16 μm) by laser ablation–single collector–sector field–ICP–MS using Jet sample and X skimmer cones. *International Journal of Mass Spectrometry* 456, 116394. https://doi.org/10.1016/j.ijms.2020.116394

Yuan, H., Gao, S., Liu, X., Li, H., Günther, D., Wu, F. (2004) Accurate U-Pb Age and Trace Element Determinations of Zircon by Laser Ablation-Inductively Coupled Plasma-Mass Spectrometry. *Geostandards and Geoanalytical Research* 28, 353–370. https://doi.org/10.1111/j.1751-908X.2004.tb00755.x